

# X-ray background measurements with XMM-Newton EPIC

D. H. Lumb<sup>1</sup>, R. S. Warwick<sup>2</sup>, M. Page<sup>3</sup>, and A. De Luca<sup>4,5</sup> \*

<sup>1</sup> Science Payload Technology Divn., Research and Science Support Dept. of ESA, ESTEC, 2200 AG Noordwijk, Netherlands

<sup>2</sup> X-ray Astronomy Group, University of Leicester, Leicester LE1 7RH, England

<sup>3</sup> Mullard Space Science Lab, University College London, Holmbury St Mary, England

<sup>4</sup> Istituto di Fisica Cosmica “G Occhialini”, CNR, via Bassini 15, I-20133 Milano Italy

<sup>5</sup> Università di Milano Bicocca, Dipartimento di Fisica, Piazza della Scienza 3, I-20126 Milano Italy

Received date / Accepted date

**Abstract.** We discuss the methods used to compile a high signal-to-noise dataset representative of both the instrumental and cosmic background signal measured at high galactic latitude by the XMM-Newton EPIC cameras. The characteristics of the EPIC background are described and the potential applications of the derived dataset in general science analysis are outlined. In the case of the cosmic X-ray background, the transition between a hard power-law spectrum (due to the integrated emission of unresolved, largely extragalactic, point sources) and a softer thermal spectrum (produced by hot plasma associated with the Galactic plane and halo) is unambiguously detected around  $\sim 1$  keV. We derive a value for the intensity of the power-law component of  $2.15 \pm 0.26 \cdot 10^{-11}$  erg cm<sup>-2</sup> s<sup>-1</sup> deg<sup>-2</sup> in the 2–10 keV band (Normalisation at 1keV of 11.1 photons cm<sup>-2</sup>s<sup>-1</sup>sr<sup>-1</sup> keV<sup>-1</sup>). The implication is that recent, very deep *Chandra* observations have resolved  $\sim 70 - 90\%$  of the 2–10 keV background into discrete sources. Our measurement is towards the higher end of the range of quoted background normalisations.

**Key words.** Instrumentation: detectors – X-rays: diffuse background – Surveys

## 1. Introduction

The instrumental backgrounds experienced in both the Advanced CCD Imaging Spectrometer (ACIS) on *Chandra* (Weisskopf et al. 2002) and the European Photon Imaging Camera (EPIC) on XMM-Newton are rather similar, as expected from their comparable orbits and detector technologies. These comprise of a combination of the unrejected components of direct and Compton scattered cosmic rays, and the flux of particles from the magnetosphere which are focused by the mirror system onto the detector. Especially for XMM-Newton, whose larger effective area and field of view offer some advantages for such observations, the analysis of very extended and faint objects (clusters of galaxies, for example) may be frustrated by the inability to account properly for the instrumental background signal.

A thorough understanding of this instrumental background is important for analysing the true Cosmic X-ray Background (CXB). For many years the interpretation of

the hard CXB as the integrated light of faint extragalactic X-ray sources, mostly Active Galactic Nuclei (AGN), has been hampered by the paradox that the diffuse spectrum at energies  $\gtrsim 1$  keV did not match the spectral form of the major AGN populations. Much of the *soft* diffuse X-ray background was resolved by ROSAT (in the Lockman Hole for example, Hasinger et al 1998), where the majority of individual sources have indeed been identified with AGNs. However the ROSAT energy band only marginally overlapped with the harder ( $\geq 2$  keV) band in which the spectrum of the CXB has been best determined by non-imaging missions such as HEAO-1 A2 (Garmire et al. 1992, Marshall et al. 1980).

Currently the characterisation of the faintest X-ray source populations in the 2–10 keV band is being revolutionised by observations made by the *Chandra* and XMM-Newton Observatories. Their capabilities are somewhat complementary: the unprecedented *Chandra* angular resolution (Van Speybroek et al. 1997) allows for negligible background and ultimate source detection sensitivity; while the XMM-Newton telescopes (Jansen et al. 2001) offer the largest ever focused area for unmatched photon gathering power.

The first deep field observations performed by these observatories (Giacconi et al 2001; Hasinger et al. 2001;

Send offprint requests to: D. Lumb (dlumb@rssd.esa.int)

\* This work is based on observations made with the XMM-Newton, an ESA science mission with instruments and contributions directly funded by ESA member states and the USA (NASA).

Hornschemeier et al. 2000; Mushotzky et al. 2000) have confirmed these promises. *Chandra* observations to a source limiting sensitivity of  $\sim 2 \times 10^{-16} \text{ erg cm}^{-2} \text{ s}^{-1}$  (0.5–2 keV) resolved  $\sim 80\%$  of the background, and found many hard spectra at faint levels, thus providing the solution of the “spectral paradox” (namely the difference between the spectrum of the background and the spectrum of bright AGN). Hornschemeier et al. 2000 also note an increase in the proportion of normal galaxies at flux levels  $\leq 3 \times 10^{-16} \text{ erg cm}^{-2} \text{ s}^{-1}$ . XMM-Newton pushed the limits further than *Chandra* in the 5–10 keV band, reaching  $2.4 \times 10^{-15} \text{ erg cm}^{-2} \text{ s}^{-1}$  (Hasinger et al. 2001). A definitive statement about the *fraction* of background resolved depends upon solving a long-standing problem concerning a discrepancy of 30% between different measurements of background normalization (e.g. Marshall et al. 1980; McCammon & Sanders 1990; Garmire et al. 1992; Vecchi et al. 1999).

In the soft X-ray regime ( $\leq 1 \text{ keV}$ ), there is a substantial Galactic contribution to the diffuse background originating from hot plasma in the Local Hot Bubble, the Galactic Disk and the Galactic Halo. The integrated spectra of these components vary over the sky due to large scale spatial structure and varying amounts of absorption. In addition there may be a more uniform component arising from an extragalactic hot intergalactic gas phase (e.g. Cen & Ostriker 1999).

Here we describe a set of template background data sets compiled from high galactic latitude pointings of the EPIC cameras on XMM-Newton. We discuss the main features of the observed background and the problems the background poses for extended source analysis. Finally we compare our results with previous measurements of the spectrum and normalisation of the diffuse cosmic X-ray background.

## 2. EPIC

The three co-aligned mirror modules of XMM-Newton each have an imaging camera at their focus, provided by the EPIC consortium. These comprise two different technologies: a conventional CMOS CCD-based imager enhanced for X-ray sensitivity (Turner et al. 2001) and a pn junction technology multilinear CCD camera (Strüder et al. 2001). The first type is located behind the two mirror modules containing Reflection Grating Arrays. Each comprise of 7 individual CCDs, closely butted, with a pixel size of  $\sim 1 \text{ arcsec}$ . The PN camera is located behind the third, unobscured telescope. It comprises an array of 12 CCDs in a monolithic silicon array - its pixels subtend about 4 arcseconds square.

The cameras offer angular resolution determined by the telescopes Full Width at Half Max (FWHM) of 5 arcsec, a field of view nearly  $30'$  in diameter, energy resolution of typically 100 eV (FWHM) and an energy range  $\sim 0.2\text{--}10 \text{ keV}$ . Each camera is provided with a set of optical blocking filters to reject possible contamination by visible light photons. On-board electronics select events

above a certain threshold and transmit data in the form of a serial list of event locations and energies.

## 3. Data Selection

### 3.1. Field Locations

For previous missions (e.g. ROSAT, Plucinsky et al. 1993 and ASCA, Gendreau et al. 1995) a measure of the internal background components was attempted with data collected while the instruments were pointed at the dark hemisphere of the Earth. Subsequent analyses of representative sky backgrounds were also made by compiling data from nominally source-free fields.

The XMM-Newton pointing restrictions, determined by the solar array or attitude measurement sub-systems, prevent accumulation of data from the dark Earth or Moon. Initial concerns about unrepresentative camera shielding configuration led us to believe that data collected with a closed instrument door would not be useful for internal background characterisation, particularly with respect to fluorescent line emission. However, we are currently compiling observations with a closed filter position, and initial results seem promising (albeit with low observational efficiency and hence low signal-to-noise at present). In the meantime we resorted to compiling data from blank sky fields. To do so with realistic signal-to-noise ratios for each of 4 major instrument modes would impose an unacceptable penalty on usable Guest Observer science programme time, therefore we concentrate on the Full Frame imaging modes which are generally used for the faint extended objects and which are our primary concern. We considered that to minimise statistical uncertainties, the effective exposure duration in our data sets should be an order of magnitude longer than that of the typical Guest Observer exposure ( $\sim 30 \text{ ks}$ ). Again, it was an unrealistic proposition to observe with the 3 EPIC optical blocking filters for  $\sim 300 \text{ ks}$  each, specifically to obtain these data. Therefore we decided to make use of a variety of Guaranteed and Calibration Time observations of “blank” fields to compile our data serendipitously. Co-addition of the multiple fields allows us to minimise any effects of “cosmic variance” resulting from pathological field sources or variations in the local diffuse X-ray emission. In addition, any time variability in the instrument behaviour will be diluted.

It was found that suitable fields were almost all taken with the filter in the THIN position, as this choice gives the maximum detection efficiency when there are no bright optical objects in the field. Whilst imposing a requirement for the THIN filter enhances the ability to obtain a homogeneous data set, it does impose additional complications for those users who have chosen to use a thicker optical blocking filter in their own observations yet still need a reliable set of background templates (see Sect. 6). Nevertheless as the soft diffuse X-ray component is more spatially and spectrally variable than the harder X-ray

emission components this was not the major driver for our analysis.

Table 1 summarises the location of the fields selected.

### 3.2. Data Generation

The data sets were processed using the pipeline processing of XMM-Newton Science Analysis Subsystem 5.2 (SAS), in order to generate calibrated event lists for each EPIC camera. Part of this standard processing removes the effects of bad pixels detected within the observation. Although many of these are fixed in location on the detector (and hence may be present in a Guest Observer’s data set), occasionally a pixel will become temporarily bad (repeated low level signals unrelated to X-ray events). These were removed from an individual observation where the repetition was typically greater than 0.5–1% of CCD readouts. (see Sect. 6)

The signatures of most cosmic ray events are removed within the instrument before transmission of data to ground. To account properly for the “dead time” effect of detector areas affected by cosmic rays, and therefore not available for detection of valid X-rays, a correction factor is calculated within SAS, based on a housekeeping parameter which counts the number of over-threshold pixels per frame, which is then normalised according to previous analysis of the average size of cosmic ray events observed in the directly transmitted images collected early in the mission.

An important background component which was not properly anticipated before launch, is a flux of low energy particles (believed to be protons) which can be focused by the mirror systems onto the detectors. Within the magnetosphere the spacecraft occasionally encounters concentrated “clouds” of accelerated particles. Their signature in the detectors is of bursts of events with few keV energy deposition that are stopped within one CCD pixel. The intensity can reach more than 100 times the quiescent background rate during the worst of “proton flares”, and these intervals are essentially unusable for analysis of faint extended objects. We removed such occurrences in our dataset by using a screening procedure based on the measured count rate of high energy single pixel events ( $\geq 10$  keV). Histograms of such events collected in time bins of  $\sim 100$ s were made and data intervals with count rates  $\geq 45$  (20) events/bin in PN (MOS) are rejected (see Fig. 1).

Concerns that in this high altitude orbit, a low level of protons might continually be illuminating the mirrors, have been allayed with the information gained from Chandra observations of the Dark Moon. In this case the recovered spectra are statistically identical with a large selection of observations made with ACIS outside the Chandra focal point (Biller et al 2002).

Next, we removed the signature of bright field sources. For each cleaned exposure an image was formed in the 0.5–

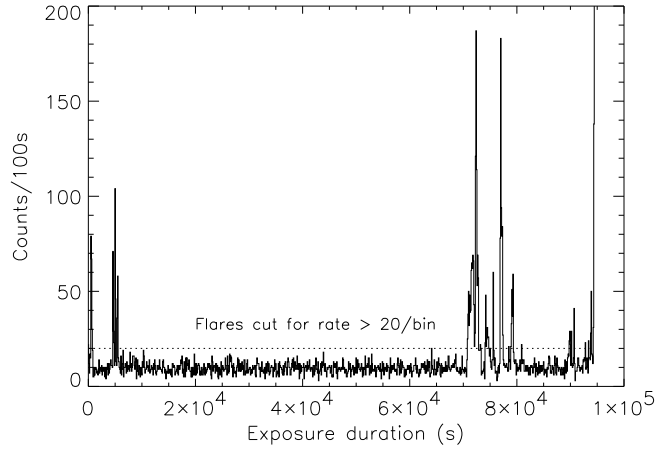


**Fig. 1.** The light curve of the high energy ( $\geq 10$  keV) particle events detected in the MOS camera during a typical observation. Intervals with count rates above 20 per 100 s bin were rejected.

2 keV band (which is devoid of most image artefacts). The SAS task *EBOXDETECT* was used to perform a simple sliding-box point source detection, without an exposure map, with a box size of  $12''$  and a task detection threshold of  $\sim 30$ – $40$ . Depending on the content of each field, approximately 10 objects per field were identified and a circular exclusion region of  $25''$  radius was applied at each source position. The resulting source-exclusion threshold cannot be directly associated with a source flux level, but nevertheless analysis of the individual fields confirmed the estimate, based on published LogN-LogS curves (Hasinger et al. 2001), that the cores of sources of flux brighter than about  $1 - 2 \cdot 10^{-14}$  erg cm $^{-2}$  s $^{-1}$  (0.5–2 keV) have been excised. According to the latest telescope PSF calibrations the above process fails to remove about 10 – 20% of their flux (almost energy independent), implying about  $4 \cdot 10^{-13}$  erg cm $^{-2}$  s $^{-1}$  deg $^{-2}$  of the bright point source flux (2 – 10 keV) remains. This is addressed in Sect. 5.3.

It should be noted that where there is no coincidence of point sources from field to field, this excision would lead to a local depression of counts in the final data set at only the 10–15% level. Conversely a suppression of the remaining brightest sources by the co-added fields leads to a similar level of dilution.

Finally the screened data were co-added, and the exposure and GTI (*Good Time Interval*) extensions of the FITS data files carefully added together so that an event list suitable for use by the XMM-Newton SAS and other standard X-ray analysis tools (e.g., XSPEC) was created. At the time of writing, these data sets are available from the XMM-Newton Science Operations Centre ftp site <ftp://xmm.vilspa.esa.es/pub/ccf/constituents>.

We noted that, despite the above standard recipe for filtering proton flares, the background rate as measured in the 1–10 keV band exhibited some remnant flares. This implies that at the lower energies, the proton flares can

RA (2000)	Dec (2000)	Date of observation	Duration (ks)	$N_H$ ( $10^{20}$ atoms $\text{cm}^{-2}$ )	$L_{II}$	$B_{II}$
02:18:00	-05:00:00	2000 July 31	60	2.5	169.7	-59.8
02:19:36	-05:00:00	2000 August 4	60	2.55	170.35	-59.5
02:25:20	-05:10:00	2001 July 3	25	2.7	172.3	-58.6
02:28:00	-05:10:00	2001 July 6	25	2.7	173.5	-58.2
10:52:44	+57:28:59	2000 April 29	70	0.56	149.3	53.1
12:36:57	+62:13:30	2001 June 1	90	1.5	125.9	54.8
13:34:37	+37:54:44	2001 June 23	80	0.83	85.6	75.9
22:15:31	-17:44:05	2000 November 18	55	2.3	39.3	-52.9

**Table 1.** Summary of target locations compiled. The co-ordinates refer to the nominal centre of the field of view.

turn on or off at a different rate to the main flare component. We attribute this to the existence of lower energy protons at the edges of the encountered proton “clouds”. We have not chosen to force further stringent data cuts in the background template files, so as to allow the general observer the option of applying additional selection on the template files so as to match his/her own requirements. However it was found that in analysing the spectrum of diffuse X-rays in the field, the recovered spectral slopes steepened with more stringent flare mitigation. Therefore before performing the spectral analysis described in Sect. 5 we repeated the filtering procedure but with an energy range of 1 – 10 keV and a count rate threshold of  $\lesssim 1.15 \text{ s}^{-1}$  for the MOS cameras.

## 4. Data Characteristics

The useful exposure time collected is about 400 ks. With such high signal-to-noise it becomes possible to identify some peculiar instrumental features. These are worthy of note since it will be important to take these into account in science analysis.

### 4.1. Fluorescent Emission Lines

The passage of charged particles through the cameras is associated with generation of fluorescent X-ray emission. This emission is most clearly seen in the form of emission lines with energies characteristic of the camera body materials (Al and stainless steel components for example). The construction of the two EPIC camera types is quite different, leading to substantially different manifestations of these features. Figs. 2 and 3 show coarse binned images of a MOS camera in bands centred around the energies of Al K and Si K emission respectively. The outer 6 of 7 CCDs detect more Al K radiation due to their closer proximity to the Al camera housing. Si K emission however is concentrated along the edges of some CCDs. This is attributed to detection of Si K X-rays escaping from the back substrate of a neighbouring CCD placed slightly forward and overlapping the subject chip. (This physical stacking arrangement of the CCDs was necessary to maximise their close packing to reduce dead space between the arrays). Finally there are a number of much less intense emission line features at higher energies (Cr, Mn,

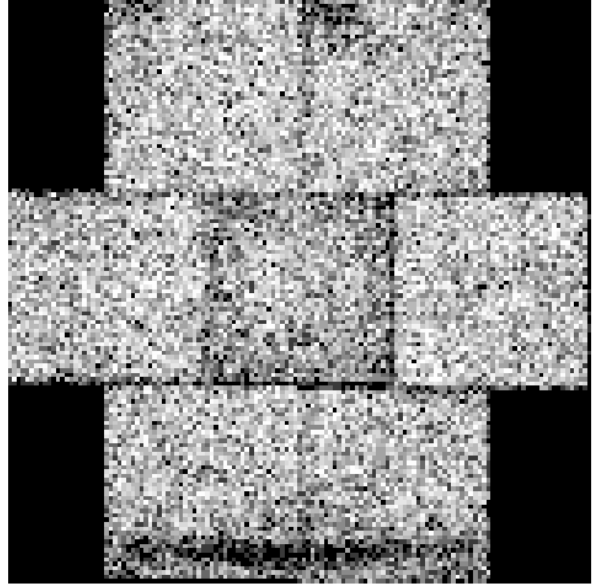


**Fig. 2.** Image from the MOS camera formed in the energy band of Al K fluorescent emission. Gaps between the chips are barely visible but some shadowing features at the top and bottom are evident (due to cut outs in the camera body for internal calibration sources). The rim areas of the central CCD are significantly dimmer than those of surrounding chips, because the CCD lies slightly below the others, and there is thus shadowing of any emission from the camera body above the focal plane.

Fe K and Au L lines for example, see Fig. 4) generated by trace elements of the camera metal bodies. In contrast the PN camera is monolithic and planar, so sees no Si K emission which is self absorbed in the large pixel ( $150 \mu\text{m}$ ) dimensions. In addition to the Al K background there is a relatively intense contribution from energies around the Cu K line of 8.048 keV (Fig. 5). What is especially notable is that this emission is spatially variable (Fig. 6). The central “hole” mirrors rather precisely the construction of the printed circuit board carrier on which the CCD array is mounted.

The consequences of ignoring the spatial variation of these background features could be dramatic. XMM-Newton is possibly the observatory of choice for spectrally-

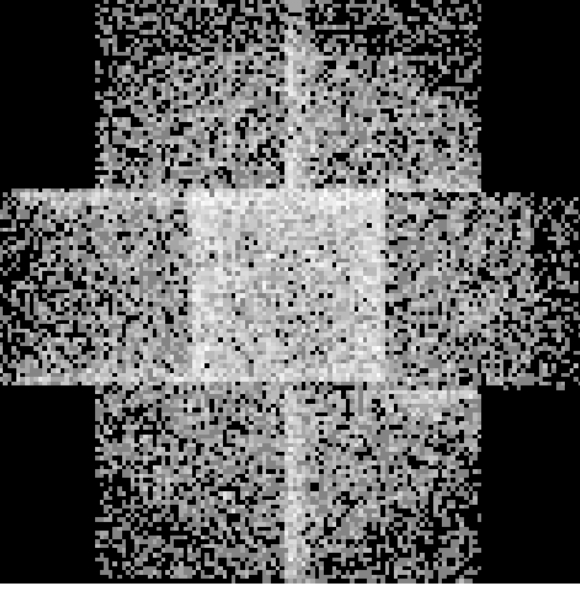


**Fig. 3.** Image from the MOS camera formed in the energy band of Si K fluorescent emission. The image is brighter along the inter-chip gaps due to the collection of Si K photons from the rear of chips which are located above their neighbours.

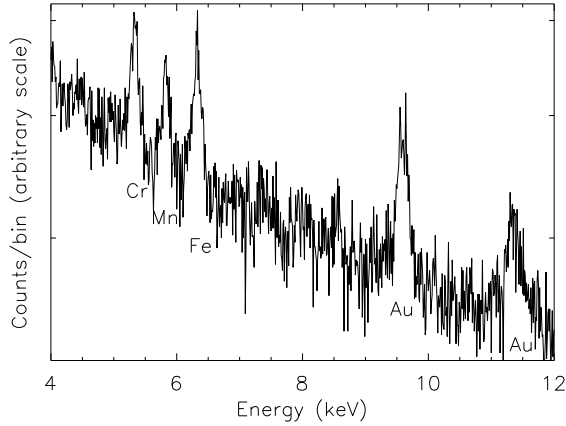


**Fig. 4.** Background spectrum from the MOS camera showing fluorescent emission from the camera body materials.

resolved imaging of large clusters, for example to map radial temperature and element distributions. However, the variable Al and Si background lines could compromise abundance determinations of cluster emission lines with moderate redshifts, while the variable high energy background would bias temperature measurements at large radii. These difficulties should be alleviated if the proposed background templates prove to be representative.

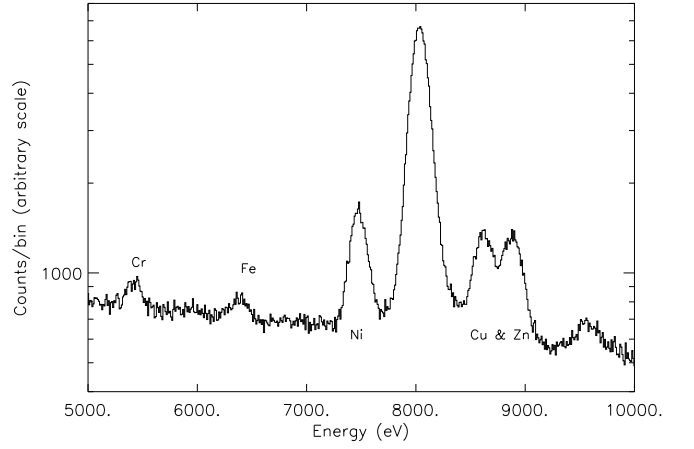


**Fig. 5.** Spectrum from the PN camera around the region of the Cu K 8.05 keV emission line, showing fluorescent emission from other camera body materials.

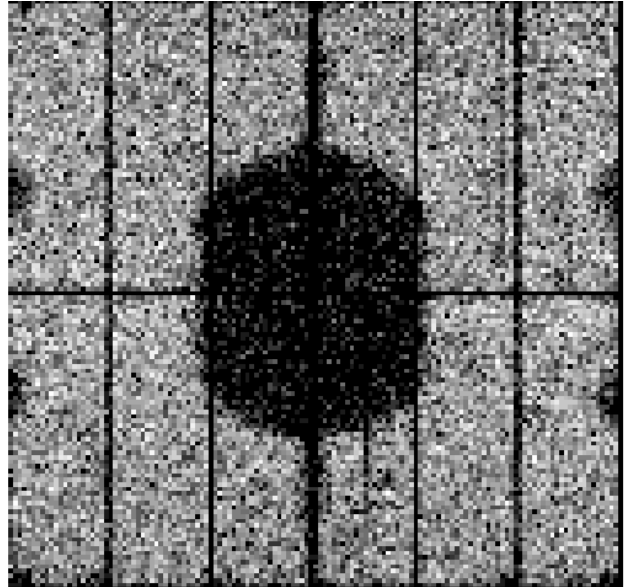


**Fig. 6.** Image from the PN camera formed in the energy band of Cu K fluorescent emission. Vertically and horizontally we see gaps where edge pixels have been removed.

#### 4.2. Unrejected Particle Background

The charged particle induced events which are not rejected by the on-board or ground processing give rise to a background component that is relatively constant in spectrum and which shows little variation across the detector.

A detailed study of the XMM-Newton background environment has been carried out (Dyer et al 1995). Using the CREME software (Adams et al 1981), the XMM-Newton operational orbit (60,000 – 100,000 km) was predicted to experience close to interplanetary galactic cosmic ray spectra at solar minimum conditions. A raw rate of  $4.4 \text{ cm}^{-2} \text{ s}^{-1}$  would reduce by a factor  $\sim 2$  at solar maximum.

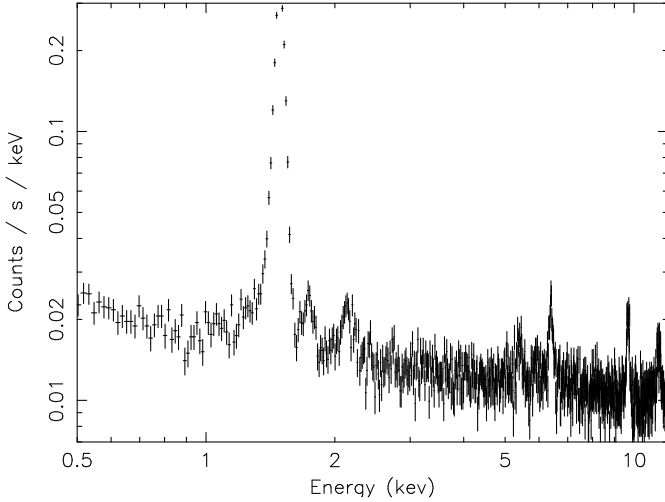


**Fig. 7.** Spectrum from the MOS camera in the region outside the field of view. The flat spectrum is consistent with 99% rejection of cosmic ray events.

Geomagnetic shielding has a small attenuation effect on the protons in the XMM-Newton orbit, below a few hundred MeV, but this affects the *total* fluence at less than 10%. The measured rates in all the 3 different sorts of CCD cameras on XMM-Newton (including the CCDs in the RGS instrument) since launch are in the range  $2\text{--}2.5\text{ cm}^{-2}\text{ s}^{-1}$ , which is entirely consistent with the expected solar modulation of the cosmic ray rate.

The mean charge deposition in both EPIC cameras due to minimally ionising particles should be  $\gg 10\text{ keV}$  per particle and, with such events typically crossing multiple pixels, the signature of the charged particles should be easy to distinguish from valid X-ray events. Actually, due to the Landau energy distribution of deposited energy the rejection efficiency is expected to be  $\sim 99\%$  in the MOS cameras (Lumb & Holland 1988). There is also a component expected from the secondary  $\gamma$ -rays and  $e^-$  excited by the particle interactions in the surrounding spacecraft.

In the case of the MOS devices, there is a substantial active CCD area outside the nominal field of view defined by the optical blocking filter. In this region one can assume that there are no contributions from sky photons or soft protons focused by the mirrors, and this should represent the true internal background. Fig. 7 shows this measured internal spectrum in the MOS1 camera below 10 keV (outside the field of view). In this regime the remnant count rate after selection for X-ray event characteristics (the SAS attributes (`#XMMEA_EM&&PATTERN` in `[0:12]`)) is  $0.026\text{ events cm}^{-2}\text{ s}^{-1}$ . Of this  $0.021 \pm 0.002\text{ cm}^{-2}\text{ s}^{-1}$  is in the flat spectrum component with the remainder in emission line components and a noise component which increases to lower energies. The flat spectrum count rate implies a rejection efficiency of  $\sim 99\%$ , as expected.

For the PN camera the flat spectrum component is about twice the intensity of the MOS cameras. We at-

tribute this to signals from the end of cosmic ray tracks that are outside the spatial rejection mask, and deposit relatively small energy signature in single pixels.

### 4.3. Low-Energy Artefacts

The most obvious features in the lowest energy band are effects of “bad pixels”. In their simplest manifestation these represent a pixel location where a small amount of leakage current is integrated during the CCD frame accumulation time; this small signal is indistinguishable from the signal generated by a valid X-ray event. A pixel which is consistently bad is flagged for removal on-board by loading a table of positions to be blanked out. Occasionally a pixel can enter the transmitted data stream before it is identified as bad. More likely, some pixels “flicker” on and off (Hopkinson 1992) with low recurrence rate ( $\leq 1\%$ ), and the efficiency for finding them post-facto in the SAS pipeline is dependent on many factors, so that some such events may occur in the background template and not the observer’s data set and vice versa.

There are additional features peculiar to each camera type. In the MOS there is a form of electronic interference noise, which causes patterns of spurious low energy events which repeat every 64 columns. Fortunately their signature is easily recognised and removed by the SAS pipeline in almost all observations. Also there are occasions when a pixel will “light up” for several successive frames. This effect is attributed to the trapping of a large signal from a cosmic ray event, which subsequently is released to the pixel site over many seconds.

In the PN camera there are occasional blocks of bright pixels, typically 4 pixels in extent, along the readout direction. Their presence varies from observation to observation. They arise from an artefact of the CCD offset bias level calculation at the start of each observation: To calculate the precise local zero signal level the average value for each pixel is determined from typically 100 readouts. Although extreme high value samples are excluded from the calculation, a local excess (due to cosmic ray detection for example) may occur during more readouts. Highly ionising events may also cause an electronic baseline droop, creating a local decrement in the calculated tables. The effect of one discrepant sample of value several keV, averaged over 100 samples is still enough to cause a noticeable shift in the locally applied detection threshold. The actual readout and calculation is performed in sets of 4 CCD rows at a time, and thus repeated blocks of typically 3-by-4 pixels might be expected to exceed the threshold during the subsequent science exposure readouts, with much higher probability than normal.

For energies  $\leq 200\text{ eV}$  there is evidence of streaks at the edge and near the middle of the array. Some of these can be attributed to the same occurrences of electronic baseline droop, and/or charge transfer loss in readout that cause a false event signature (especially occurring in the first few pixels of the next frame readout).

## 5. Spectral Analysis

### 5.1. Internal Background

The high signal-to-noise data set described allows the diffuse X-ray background parameters to be compared with the estimates made using other observatories. In this work we restrict ourselves to analysis with the MOS cameras only, because the spatio-spectral complications of the internal background can be reasonably well corrected using data from outside the focal plane area. Similar subtraction in the PN camera will be the subject of further work, when sufficient internal background data can be collected during the on-going calibration programme. Furthermore, the MOS CCDs have nearly identical responses across the focal plane, and the average response can be determined by application of a simple mirror vignetting correction. Conversely for the PN, the response varies along each CCD due to the effects of charge transfer inefficiency, and the determination of a linear change in response with position and a radial vignetting function requires a rather complicated weighting function which is still under development.

However, even in the case of the MOS, analysis using the normal technique of an area-scaled background subtraction was complicated. It was found that e.g., the rather variable Al & Si emission line intensities have an associated component of redistribution of photon signal to lower energies. The intensity outside the FOV is clearly different than inside the field, and therefore, even “ignoring” the Al K line region from fitting process, after subtraction, would significantly distort the whole sub-keV spectral region. Similar arguments, but with less dramatic magnitude, apply to the other internal fluorescent lines. In Fig. 8 we show the comparison of the internal background component from *outside* the field of view (but scaled with appropriate area correction) with the total spectrum (including the CXB) from the central field of the detector (specifically a central  $\sim 13$  arcminutes radius region). The internal component dominating above 5 keV seems to be scaled correctly via the ratio of in- and out-of-field detector areas, but the emission line intensities at Al K and Si K require a different scaling (this is partly masked by the diffuse cosmic X-ray background component) consistent with spatial variations noted earlier. Therefore we decided to model the internal background, with multiple Gaussian functions to characterise these emission lines, superimposed upon a broken power-law to describe the continuum due to unrejected particle backgrounds, and low energy noise. The hard component of unrejected cosmic rays manifests as a power law of counts versus energy of  $\sim E^{-0.2}$ , turning up at about 1 keV to a power law  $\sim E^{-0.8}$  (this is very similar in form to models used to describe internal background in the ASCA CCD cameras). In the spectral fitting described below, the fluorescent emission line energies and widths were fixed to the values determined in the out-of-field component but the normalisations of the lines were allowed to vary to com-

pensate for spatial variations. The normalisation of the broken power-law component was fixed according to the ratio of the collection areas.

Yet a further complication is that the charged particle events are collected unevenly across the array. After collection in the image area the data are shifted rapidly into a shielded store section, and read-out relatively slowly ( $\sim 2.6$  s) so that rows farthest from the readout node spend  $\sim 50\%$  longer in the array. The pixel size in the store section is less than  $1/3$  of the physical size of pixels in the image section, so the actual range in equivalent accumulation times is  $\sim 15\%$ . In addition the smaller pixel size allows for a much enhanced rejection ratio to particle events collected during the store readout than those collected in the image section. As a consequence of the orthogonal readout organization of the MOS CCDs, only 2 of the 6 outer CCDs have a potential spatial bias in this cosmic ray collection efficiency, hence the expected normalization error in the unrejected cosmic ray component is  $\ll 5\%$ . We confirmed this spatial invariance by examining a selection of data sets taken with the CLOSED filter position, and indeed find no evidence for a large spatial variation in the background *except* in the fluorescent emission lines.

At energies  $\leq 5$  keV the CXB dominates, with a clear signature of low energy emission lines at  $E \leq 1$  keV, which are not present in the internal background but most likely originate in Galactic thermal emission.

### 5.2. Cosmic X-ray Background

Using the spectral model of the internal background described in the previous section, we have proceeded to fit the *full background spectrum* measured in the EPIC MOS cameras by including additional spectral components representative of the diffuse CXB. Specifically we adopt an empirical CXB model consisting of two optically-thin thermal components (MEKAL, Mewe et al. 1985) plus a power-law component. The former represent the soft CXB produced by hot plasma located in the Galactic disk and halo whereas the latter models the hard CXB of extragalactic origin which, most likely, is due to the integrated emission of faint unresolved AGN.

Other details of the spectral analysis are as follows. Since the metallicity of the thermal component could not be well constrained, the plasma abundances were fixed at solar (Anders & Grevesse 1989). Also the exposure time weighted hydrogen column density (Dickey & Lockman 1990) averaged over all our fields was calculated to be  $1.7 \times 10^{20} \text{ cm}^{-2}$  and fixed at this value. We have considered an overall estimate of 2% systematic error is appropriate to characterize the current level of calibration accuracy, except for the region around the O absorption edge feature in the CCD detection efficiency, to which we assign a 5% systematic uncertainty (450 eV–600 eV). All spectral bins below an energy of 200 eV were excluded.

In the spectral fitting we use response functions which account for the average effective area, weighted accord-

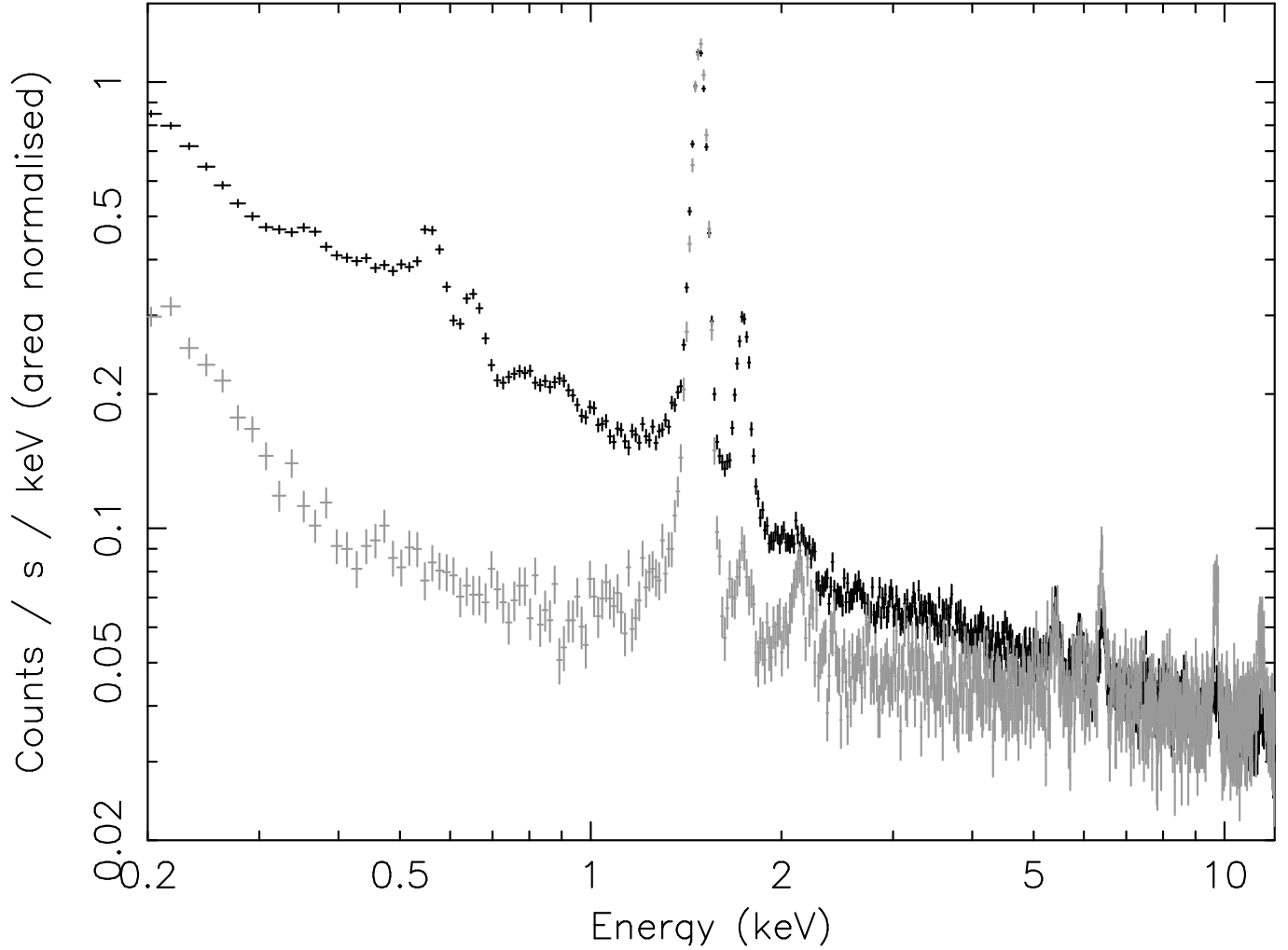


**Fig. 8.** Comparison of the internal background (grey) and total background spectrum (black) in MOS 1 camera.

ing to off-axis angle. The vignetting calibration of the MOS cameras is complicated by an understanding of the azimuthal dependence of the blocking fraction of the Reflection Grating Spectrometer array (den Herder et al. 2001) modules in their telescope beams. Nevertheless as we have azimuthally *averaged* this factor in these observations, we believe that the uncertainty of the vignetting function measurement ( $\sim 1.5\%$  for  $E \leq 8\text{ keV}$  at  $10.5$  arcminute field angle - Lumb et al. 2002) represents an upper limit to the uncertainty on the average effective area weighting applied in the analysis.

Fig. 10 shows the measured CXB spectrum (after subtracting the best-estimated of the internal background) in the  $0.2\text{--}10\text{ keV}$  band, our derived best-fitting CXB spectral model and the fitting residuals. The corresponding parameter values plus errors are summarised in Table 2. The reduced  $\chi^2$  of the fit was  $\chi^2_\nu = 1.17$  (566 degrees of freedom).

The background normalisations quoted in Table 2 ignore the contribution of out-of-field scattered X-rays. X-rays at angles  $\sim 1$  degree off axis have a small probability

of reaching the focal plane after only one reflection (off the hyperbola mirror) rather than a true focus from the double reflection geometry. For example, such effects were a considerable complication in the ASCA observatory since they gave rise to roughly 30% of the signal. In XMM-Newton, considerable effort was put into designing a baffle which minimizes this effect. Ground measurements at optical wavelengths have confirmed its efficiency. At the time of writing the detailed in-orbit X-ray calibration is incomplete. However measurements of the Crab Nebula observed off-axis, show that the X-ray leak is within a factor of 2 of predicted ( $1.5 \cdot 10^{-3}$ ). With a rather small energy dependence ( $\sim \pm 20\%$  from  $1\text{--}10\text{ keV}$ ) of the X-ray leak, this leads us to estimate that the contribution of diffuse flux gathered from out-of-field angles of  $0.4\text{--}1.4$  degrees is of order 7% of the true focused in-field signal, and the associated systematic error (due largely to the energy dependence) is  $\pm 2\%$ .



### 5.3. Extragalactic Cosmic X-ray Background

The hard power-law component representing the extragalactic CXB has a measured photon index of  $\Gamma = 1.42 \pm 0.03$  (90% confidence limits for one parameter) with a normalisation at 1 keV of  $8.44 \pm 0.24$  photon  $\text{cm}^{-2} \text{s}^{-1} \text{keV}^{-1} \text{sr}^{-1}$  (corrected for out-of-field scattering). The corresponding 2–10 keV flux per square degree is  $1.64 \cdot 10^{-11} \text{ erg cm}^{-2} \text{s}^{-1} \text{deg}^{-2}$ .

Fig. 9 shows the contribution of the power-law component to the whole spectrum; the residuals illustrate very clearly that the breakpoint between the hard extragalactic power-law and the soft CXB emission of Galactic origin occurs close to 1 keV. This is a spectral range where many instrument technologies overlap. For example, missions flown in the past utilising either thick-windowed collimated gas proportional counters or X-ray imagers with CCDs were mainly sensitive above  $\sim 1$  keV. Conversely, the telescope and thin-windowed proportional counters of ROSAT were tuned to the detection of X-rays below  $\sim 2$  keV. Nevertheless, considerable evidence has accumulated for a soft excess of Galactic origin in the CXB spectrum (eg. Bunner et al. 1971; Garmire et al. 1992). The fact that the EPIC cameras identify the spectral break in the CXB in such a convincingly and unambiguous fashion does, however, demonstrate the importance of broad spectral coverage for CXB measurements. Presumably limited bandpass/energy leverage has also been a factor in producing discrepancies of up to 30% in published estimates of the normalisation of the extragalactic background.

In order to compare our background measurements with other all-sky averages (e.g. Della Ceca et al. 1999) we must account for the bright source component that has been removed from our data (*i.e. the bright resolved sources that we have specifically excluded from our summed spectra*). Currently the most secure 2–10 keV source count data in the bright source regime comes from ASCA and BeppoSax. We have used the log N - log S curves of both Ueda et al. (1999) and Cagnoni et al. (1998) for the 2–10 keV band. We convert our lower flux limit (for the excluded sources) from the 0.5–2 keV band to 2–10 keV via an AGN spectrum appropriate to the flux range ( $\Gamma \sim 1.7$ ). Thus we integrate the counts from  $3 \cdot 10^{-14}$  to  $10^{-12} \text{ erg cm}^{-2} \text{s}^{-1}$  (2–10 keV). This leads to a bright source correction factor of  $6.0 \cdot 10^{-12} \text{ erg cm}^{-2} \text{s}^{-1} \text{deg}^{-2}$ . The estimated uncertainty in that value is driven by the possible range of 2 in the lowest flux from which we integrate the source counts ( $\sim 2 - 4 \cdot 10^{-14} \text{ erg cm}^{-2} \text{s}^{-1}$  in 2–10 keV), and is estimated to be  $2.0 \cdot 10^{-12} \text{ erg cm}^{-2} \text{s}^{-1} \text{deg}^{-2}$ .

When we combine our unresolved hard CXB intensity with the estimated contribution of bright sources we obtain a value for the total intensity of the hard CXB of  $2.15 \pm 0.26 \cdot 10^{-11} \text{ erg cm}^{-2} \text{s}^{-1} \text{deg}^{-2}$ . Table 2 lists the estimated uncertainties in computing this value.

An independent check on the derived hard CXB intensity was made using data *only* from inside the field of view. This was accomplished via maximum-likelihood fit-

Component	Value	Error	
Normalisation	9.03	0.24	ph $\text{keV}^{-1} \text{cm}^{-2} \text{s}^{-1} \text{sr}^{-1}$
Avg. Vignetting	0.68	0.01	In response fn.
Stray Light	1.07	0.02	Energy dependence
Bright Sources	6.0	2.0	$\times 10^{-12} \text{ erg cm}^{-2} \text{s}^{-1} \text{deg}^{-2}$

**Table 2.** Summary of the components, and associated error estimates, used in correcting for the final extragalactic background normalisation

ting (Crawford et al 1970) of vignettted and unvignettted components to the measured spatial distribution of events over the field of view. In this case a fit was made for an unvignettted (cosmic-ray background) and a vignettted (true X-ray photons) image component, with a vignetting function of the form described by the XMM-Newton calibration database. Images were constructed from both MOS datasets in 150 eV wide bands, and fit individually; uncertainties were determined during the fits using the  $\Delta C$  statistic (Cash 1979). The maximum likelihood fitting was unable to constrain the vignettted component above 5 keV. The fitted intensities of the vignettted component were then averaged between the two MOS detectors, and cast as a spectrum suitable for use with XSPEC. Energy bins corresponding to the strong instrumental Al K and Si K emission lines (*i.e.* between 1.3 and 1.9 keV) and where the Galactic background is significant (below 1 keV) were excluded. A power-law fit to the spectrum of the vignettted background resulted in  $\Gamma = 1.34 \pm 0.10$  (90% confidence), consistent with the best fit value of  $\Gamma = 1.42$  obtained earlier. Fixing the slope at  $\Gamma = 1.42$ , and fitting the normalisation of our vignettted spectrum results in a value of  $A_{\Gamma} = 9.1 \pm 0.4$  photon  $\text{keV}^{-1} \text{cm}^{-2} \text{s}^{-1} \text{sr}^{-1}$  (90% confidence), in excellent agreement with the value given in Table 2.

To further validate our estimate of the corrections for missing bright source flux, we made an independent fit on the whole EPIC MOS data set with bright sources *included* and determined a 2–10 keV intensity of  $2.11 \pm 0.11 \cdot 10^{-11} \text{ erg cm}^{-2} \text{s}^{-1} \text{deg}^{-2}$ . The correction for missed bright sources is estimated in this case to be only  $\sim 1 \cdot 10^{-12} \text{ erg cm}^{-2} \text{s}^{-1} \text{deg}^{-2}$ ; thus this analysis gives a result consistent with that noted earlier. The spectral slope in this case steepens to  $\sim 1.45$ , as expected for the addition of the brighter steeper spectrum sources.

We also measured the brightest of the excluded sources, and determined it to have a flux of  $6 \cdot 10^{-13} \text{ erg cm}^{-2} \text{s}^{-1}$  (2 – 10 keV). This is consistent with the source count prediction for a total field of 1.3 square degrees, confirming that integration to higher fluxes from this point requires a minimal correction.

Our derived flux of the hard CXB signal compares well with the BeppoSAX (Vecchi et al. 1999) and Wisconsin (McCammon & Sanders 1990) values, but is somewhat higher than the HEAO-1 value (Marshall et al. 1980, although see Garmire et al. 1992). Our result implies that the fraction of the background in the 2–10 keV band

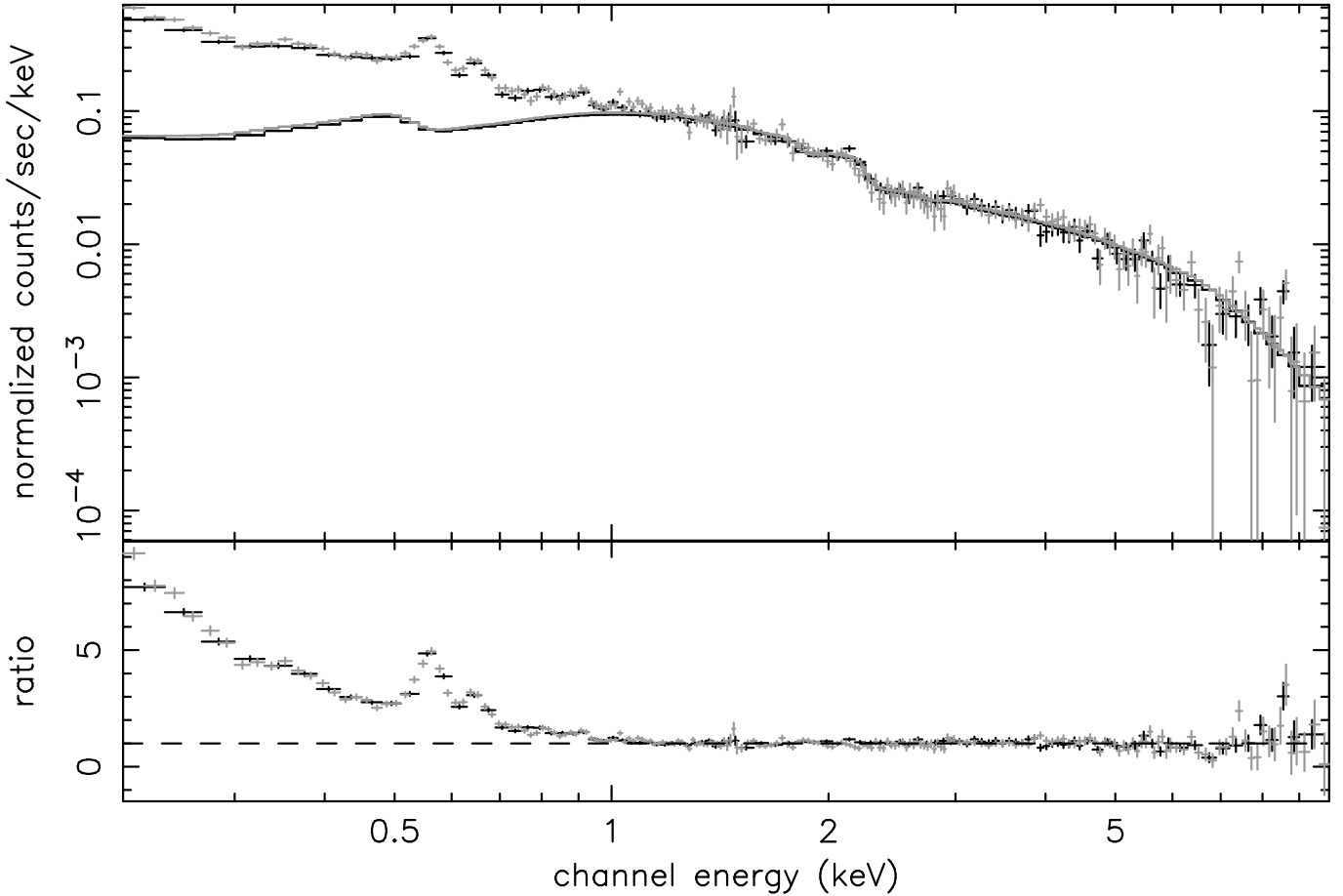


**Fig. 9.** Comparison of the overall CXB measured in the 2 MOS cameras with the power-law extragalactic component. The lower panel shows the ratio between measured background and a power law with  $\Gamma=1.42$ . At the highest energies there is evidence for poor subtraction of fluorescent emission lines in Ni, Cu and Au.

that has been resolved into discrete sources in the recent *Chandra* 1 Ms observations is  $\sim 70 - 90\%$ . This highlights the fact that estimates of the fraction of the CXB resolved into discrete sources in narrow beam surveys depend sensitively on the assumed normalisation of the CXB spectrum and the corrections applied for the contribution of bright sources (which must be deduced from wide area surveys) - see for example, Baldi et al. (2001). The effects of field-to-field cosmic variance (which as yet are largely unquantified) may also be important.

### 5.3.1. Galactic background

We find that the soft CXB spectrum is well modelled by two thermal components with temperatures of 0.07 and 0.20 keV respectively (see Table 3). Kuntz & Snowden (2000) describe a re-analysis of ROSAT survey data, utilizing different energy-band intensity ratios. For high galactic latitudes they estimated that after correction for any Local Hot Bubble component, a best fit two temperature model with  $kT = 0.099^{+0.054}_{-0.037}$  keV and  $kT = 0.24^{+0.08}_{-0.03}$  keV provided a good description of the measured ROSAT spec-

trum. This agrees within the errors of our own estimate. We note that the emission line ratios provide the key information for the temperature diagnostics, but the truncation of EPIC response below 200 eV prevents an accurate determination of the absorption columns, and the 0.25 keV emission (knowledge of which is needed to disentangle the Local Hot Bubble component from more distant disk and halo emission).

We made an estimate of the sub-keV emission in some of the different fields noting differences in the measured temperature and flux. This variability in emission and lack of detailed temperature measurement capability hampers a more accurate determination of Galactic background properties. For example, the measured mean deviation from field to field of the 2–10 keV intensity is about 3.5%, consistent with an isotropic extragalactic background. On the other hand the mean deviation of 0.2–1 keV intensity is about 35% from field to field. This is highlighted in Fig. 11 where we show the best two temperature fits to several fields, with their related deviations. It is clear that:

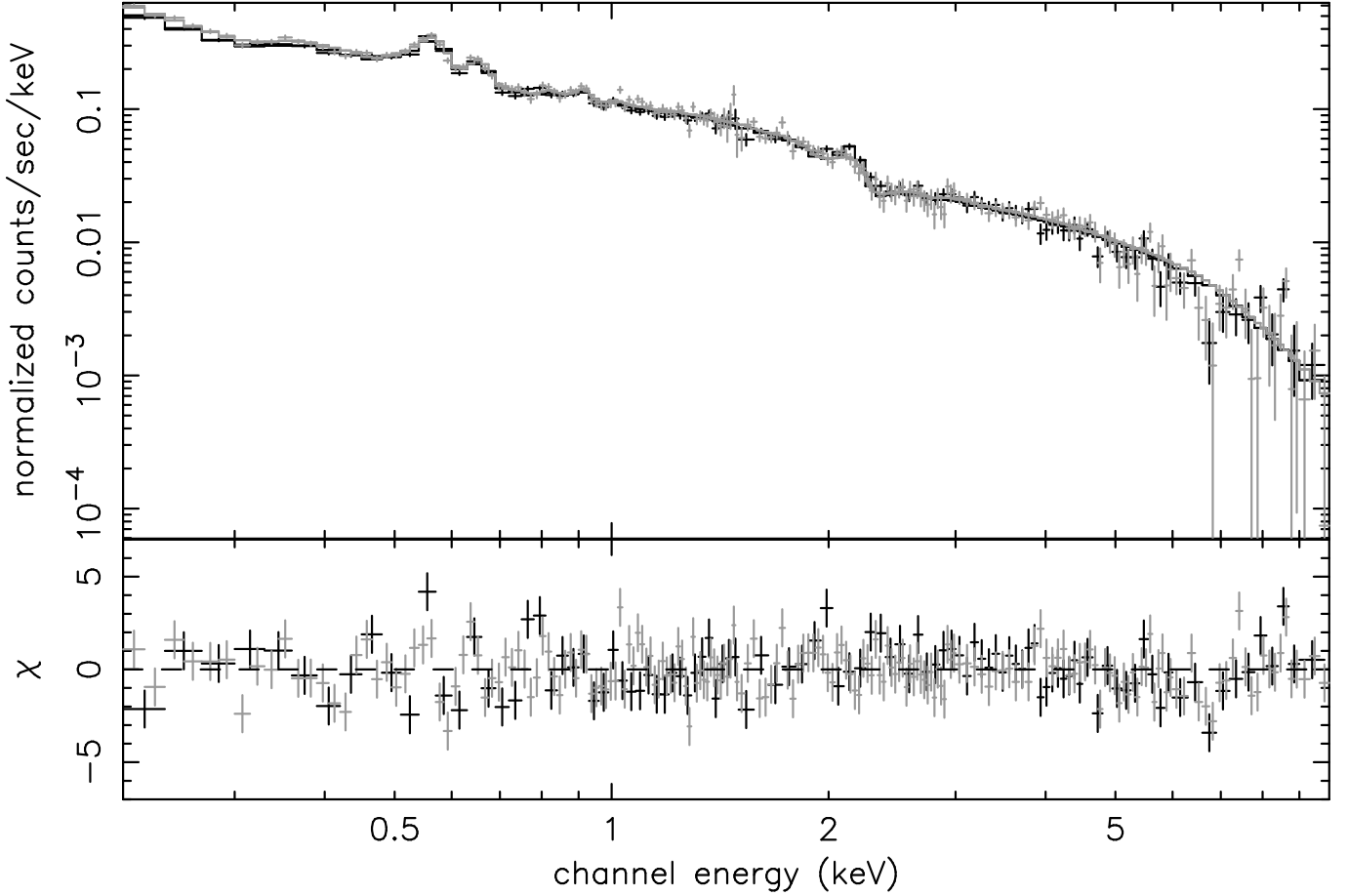


**Fig. 10.** Best fit model and residuals to the overall cosmic diffuse X-ray emission

Component	Best Fit Value	Error	
$\Gamma$	1.42	0.03	
$A_{\Gamma}$	9.03	0.24	$\text{ph keV}^{-1} \text{ cm}^{-2} \text{ s}^{-1} \text{ sr}^{-1}$
$kT_1$	0.204	0.009	keV
$A_1$	7.59	1.2	
$kT_2$	0.074	0.003	keV
$A_2$	116	32	

**Table 3.** Summary of the best fit spectral parameters derived for the cosmic diffuse background components. Normalisations are quoted per steradian, but do not include corrections for stray light and missing bright sources.

- substantially different temperatures and absorption values apply to the different fields,
- that the residuals are not coherent from one field to the next indicating that the instrument calibration is *not* the major impediment to the low energy modelling,
- a simple two temperature model is not an adequate description of the sub-keV emission.

The whole subject of determination of the soft Galactic diffuse component is beyond the scope of the current work.

## 6. Caveats for Use

The EPIC cameras allow a choice of optical blocking filter to prevent contamination by optically bright targets. For most extended and/or faint extragalactic targets, such contamination is negligible, and the thinnest filter can be employed, as indeed is the case for all the observations compiled in this work. However, if a thicker filter was used, the transmission of diffuse background X-rays (and any remnant proton flux) will be reduced. Therefore the observer should model the differences in soft component based on the response matrices and limited knowledge of the expected Galactic emission.

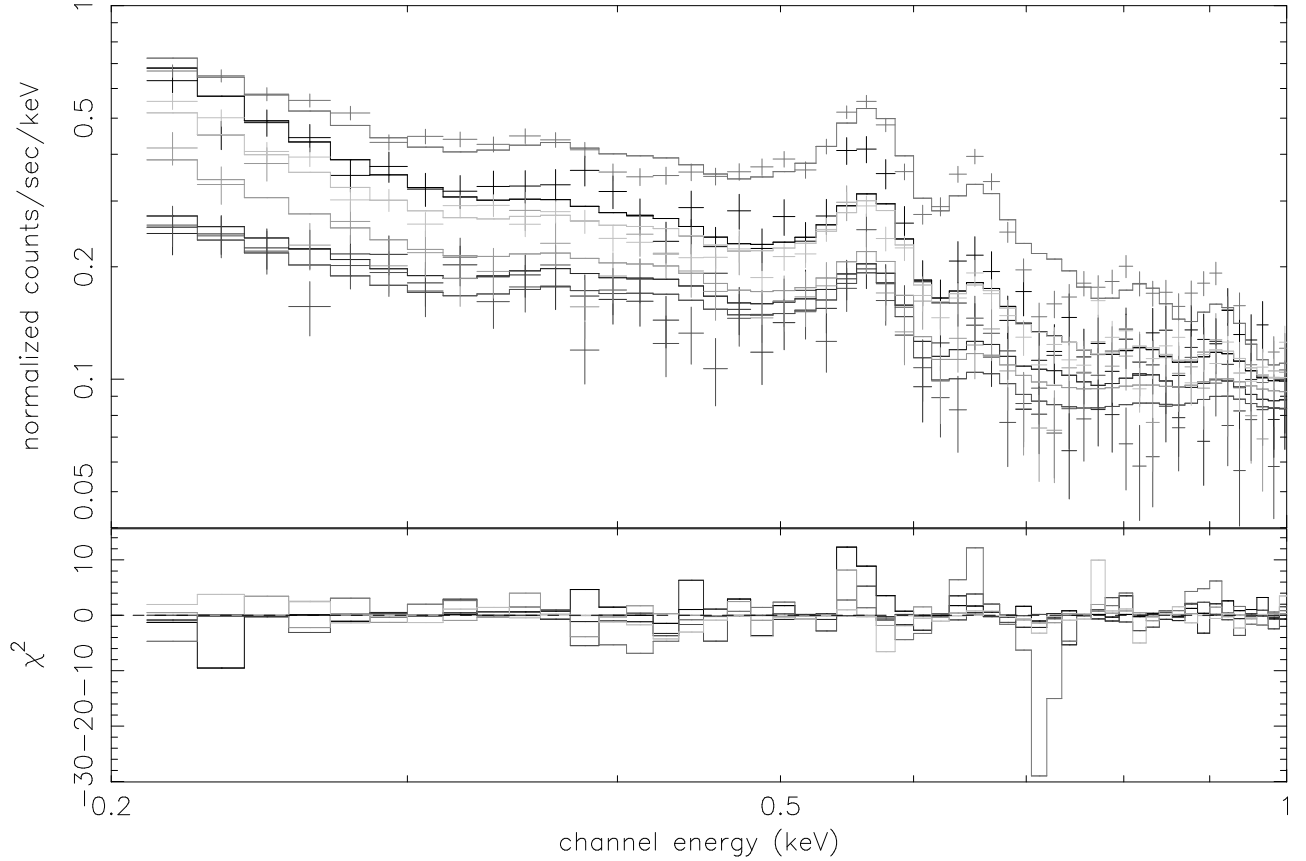


**Fig. 11.** Comparison of the sub-keV spectra of a number of fields highlighting the wide range of measured surface brightness.

The observer must take care to extract background from an appropriate location in the FOV. Most simply the extraction region should be defined in detector co-ordinates to match closely the region of the desired science target. In some applications the user would subtract data in sky co-ordinates. In this case the template event lists could be recast to mimic the nominal pointing direction of the observer’s field (for example using SAS task *ATTCALC*)

We note that despite the standard recipe for filtering proton flares, the background rate as measured in 1–10 keV bands exhibits some remnant flares. This implies that at lower energies, the proton flares turn on more slowly, yet before the main flare component. While a more restrictive proton flare screening was applied for the spectral analysis of the background, we have not chosen to apply such stringent data cuts in the background template files, so that the general observer can apply an additional selection of the template files if necessary. We emphasise that in analysing the spectrum of diffuse X-rays in the field, the recovered spectral slopes steepen with more stringent flare mitigation. Careful comparison of the recipes used for GTI creation must be made. Nevertheless, it is possible that the lowest level proton fluxes are spectrally variable, and no complete subtraction is possible.

Although point sources have been removed or significantly diluted, careful examination of the images derived from these event lists reveals significant intensity fluctuations. On scales of arcminutes appropriate to extended sources, this is not expected to be a significant problem, and indeed representative of the unresolved background. However, if the user extracts spectra from regions comparable with the mirror point spread function scale, then manual inspection is necessary to guard against variations in counts arising from treatment of point sources in the template files.

As noted previously there are particular defects to be expected in the lowest energy ( $\leq 0.3$  keV) spectral ranges. Furthermore, at the time of writing, the calibration of the EPIC soft X-ray spectral response awaits completion. The transmission of filters at energies  $\leq 250$  eV is difficult to measure, the CCDs’ calibration at the ground synchrotron facility was not performed at energies  $\leq 150$  eV and the detailed redistribution of signal from photons of energies  $\sim 1$  keV into partially collected events in the softest band was also not determined completely in ground measurements. For the time being spectral analysis below 250 eV should be treated with caution.

For the highest quality determination of the background appropriate to the observer’s own data the following steps should be employed. It is intended to pro-

vide tools within the XMM-Newton SAS environment to achieve this, but most steps can be performed manually (see for example Majerowicz & Neumann 2001 ).

- Following suitable flare screening, define a background region (B) and extract the observed spectrum ( $C_{\text{back}}$ ) from the observer’s data set. From an identical region in the template file the observed spectrum ( $T_{\text{back}}$ ) should provide a measure of variability of CR component by checking count rates for  $E \gtrsim 5$  keV and/or the fluorescent emission line normalisations.
- To estimate a better internal background spectrum for the observer’s data set ( $C_{\text{inst}}$ ), determine a predicted cosmic background spectrum for the observer’s region based on ROSAT All Sky Survey maps, hydrogen column etc.. An experimental tool is available at HEASARC web site to aid this (Sabol 2001). Create response matrices for the background region (here is where the effect of different filters can be introduced). Fold this cosmic spectrum through the response matrices to obtain a *predicted* cosmic component for the background region, ( $C_{\text{cos}}$ ).

$$C_{\text{inst}} = C_{\text{back}} - C_{\text{cos}}$$

- A similar approach with the template files showed that with a weighted average  $N_{\text{H}}$  of  $1.7 \cdot 10^{20} \text{ cm}^{-2}$ , and a 0.2 keV thermal spectrum determined from our spectral fitting, the HEASARC tool predicts a ROSAT  $R_{45}$  PSPC count rate of  $1.3 \text{ s}^{-1}$  in a  $144 \text{ arcmin}^2$  field, and a 0.47-1.21 (ROSAT band) flux of  $1.67 \cdot 10^{-11} \text{ erg cm}^{-2} \text{ s}^{-1}$ . This could likewise be used to make an estimate of the internal background of the template file region in order to better estimate the scaling factor (K) for the cosmic ray component.

$$T_{\text{inst}} = T_{\text{back}} - T_{\text{cos}} \text{ and } K \sim C_{\text{inst}}/T_{\text{inst}}$$

- Repeating the same exercise for the source region in both template and observed data sets could lead to a *predicted* background data spectrum comprising the scaled internal component, and the predicted galactic component with the appropriate filter responses.

## 7. Conclusions

Proper treatment of the background observed in the XMM-Newton EPIC cameras is very important for spectral and spatial analysis of faint extended objects. The template background files described provide a very high signal-to-noise characterisation of the high energy ( $\geq 1$  keV) background suitable for such analysis. The sub-keV background is consistent with models of the Galactic diffuse emission, but is spatially and spectrally variable, and needs indirect arguments to provide an accurate subtraction. The extragalactic power-law background component has been measured, and is consistent in measured power-law index with previous data. The normalization measured is in good agreement with, and provides an important additional constraint of the fraction of back-

ground resolved into point sources by *Chandra* and XMM-Newton.

*Acknowledgements.* All the EPIC instrument calibration team who have contributed to understanding the instrument are warmly thanked for their efforts. During early developments of the background template file activity there was helpful feedback from users of the data for analysis of PV cluster targets. We wish to record the helpful discussions with M Arnaud, U Briel, D Neumann, J Nevalainen, R Lieu and S Snowden. We thank the anonymous referee for useful comments.

## References

- Adams, J.H., Silberberg, R. & Tsao, C.H. NRL Memorandum Report, “Cosmic ray effects on microelectronics”, Naval Research Lab, Washington, USA 1981.
- Andres, E. & Grevesse, N., 1989 *Geochimica et Cosmochimica Acta* 53, 197
- Baldi, A., Molendi S., Comastri, A. et al., 2001 submitted to *ApJ astro-ph0108514*
- Biller, B., Plucinsky, P. & Edgar, R. Chandra X-ray Center Calibration memo, 01\_22\_02
- Bunner, A.N., Coleman, P.L., Kraushaar, W.L., McCammon, D., 1971, *ApJ*, 167, L3
- Cagnoni, I., della Ceca, R. & Maccacaro, T., 1998 *Ap J* 493, 54
- Cash W., 1979, *ApJ*, 228, 939
- Cen, R. & Ostriker, J. P., 1999 *ApJ* 514, 1
- Cowie, L. L., Garmire, G.P., and Bautz, M.W. et al, 2002 *Ap J* 566 L5
- Crawford D.F., Jauncey D.L., & Murdoch H.S., 1970, *ApJ*, 162, 405
- Della Ceca, R., Braito, V. and Cagnoni, I. et al., 1999, *Ap J*, 524, 674
- den Herder, J. W., Brinkman, A. C., Kahn, S. M. et al., 2001, *A&A* 365, L7
- Dickey, J. M. & Lockman, F .J. 1990, *ARAA*. 28, 215.
- Dyer, C.S., Truscott, P.R., Evans, H.E. & Peerless. C.L. Defence Research Agency Report, “Analysis of XMM instrument background induced by the radiation environment in the XMM orbit”, DRA/CIS(CIS2)/CR95032, DRA Farnborough, U.K. 1995
- Garmire, G. P., Nousek, J. A., Apparao, K. M. V. et al., 1992, *Ap J* 399, 694
- Gendreau, K., Mushotzky, R. & Fabian, A., 1995, *PASP* 47, L5
- Giacconi, R., Rosati, P., Tozzi, P. et al., 2001, *Ap J* 551, 624
- Hasinger, G., Burg, R., Giacconi, R. et al 1998 *A&A* 329, 482
- Hasinger, G., Burg, R., Giacconi, R. et al. 1993 *A&A* 275, 1
- Hasinger, G., Altieri, B., Arnaud, M. et al., 2001, *A&A* 365, L45
- Hopkinson, G.R. , 1992, *IEEE Trans Nucl Sci* 39, 2018
- Hornschemeier, A., Brandt, W. N., Garmire, G .P. et al., 2000, *ApJ* 541, 49
- Jansen, F., Lumb, D. H., Altieri, B. et al., 2001, *A&A* 365, L1
- Kuntz, K. D. & Snowden, S. L., 2000, *Ap J* 543, 195
- Lehmann, I., Hasinger, G., Schmidt, M., et al. 2001, *A&A*, 371, 833
- Lumb, D.H. & Holland, A. D., 1988, *IEEE Trans Nucl Sci* 35, 534
- Lumb, D.H., Erd, C., Finoguenov, A. et al., 2002 in preparation

- Majerowicz, S. & Neumann, D. M. in Galaxy Clusters and the High Red-shift Universe, eds D. Neumann, F. Durret & J. Tran Thanh Van - Proceedings of XXIth Moriond Astrophysics Meeting (March 2001)
- Marshall F. E., Boldt, E.A. and Holt, S.S. et al. 1980, Ap J 235, 4
- McCammon, D. & Sanders, W. T. 1990, ARA& A 28, 657
- Mewe, R., Gronenschild, E.H.B.M. & vd Oord, G. H. J., 1985, A&AS 62, 197
- Mushotzky, R., Cowie, L., Barger, A. & Arnaud, K. 2000, Nature 404, 459
- Plucinsky, P., Snowden, S., Briel, U. et al., 1993, Ap J 418, 519
- Sabol, E. available at <http://heasarc.gsfc.nasa.gov/cgi-bin/Tools/xraybg/xraybg.pl>
- Strüder, L., Briel, U., Dennerl, K. et al., 2001, A&A 365, L18
- Tozzi, P., Rosati, P., Nonino, M. et al. 2001, Ap J 562, 42
- Turner, M. J. L. T., Abbey, A., Arnaud, M. et al., 2001, A&A 365, L27
- van Speybroek, L. P., Jerius, D., Edgar, R. J. et al., 1997, Proc SPIE 3113, 89
- Ueda, Y., Takahashi, T., Inoue, H. et al., 1999, ApJ 518 656
- Vecchi, A., Molendi, S., Guainazzi, M. et al., 1999 A&A 349, L73
- Watson, M. G., Augeres, J-L., Ballet, J. et al., 2001, A&A 365 L51
- Weisskopf, M. C., Brinkman, B., Canizares, C. et al., 2002 PASP 14 iss 791, 1